



Cavity-controlled diffusion in 8-membered ring molecular sieve catalysts for shape selective strategy



Shushu Gao^{a,c,1}, Zhiqiang Liu^{b,1}, Shutao Xu^{a,*}, Anmin Zheng^{b,d,*}, Pengfei Wu^a, Bing Li^a, Xiaoshuai Yuan^a, Yingxu Wei^{a,*}, Zhongmin Liu^{a,*}

^a National Engineering Laboratory for Methanol to Olefins, Dalian National Laboratory for Clean Energy, iChem (Collaborative Innovation Center of Chemistry for Energy Materials), Dalian Institute of Chemical Physics, Chinese Academy of Sciences, Dalian 116023, P. R. China

^b State Key Laboratory of Magnetic Resonance and Atomic and Molecular Physics, National Center for Magnetic Resonance in Wuhan, Wuhan Institute of Physics and Mathematics, Chinese Academy of Sciences, Wuhan 430071, P. R. China

^c University of Chinese Academy of Sciences, Beijing 100049, P. R. China

^d School of Materials Science and Engineering, Zhengzhou University, Zhengzhou 450051, P. R. China

ARTICLE INFO

Article history:

Received 2 April 2019

Revised 4 June 2019

Accepted 1 July 2019

Available online 26 July 2019

Keywords:

Molecular sieves
Shape-selectivity
Cavity-control
Diffusion
Molecular dynamics
PFG NMR

ABSTRACT

Shape selectivity is the most important feature and advantage of molecular sieve catalysis. Diffusion of reactant and product molecules inside the confined environments with channels and cavities is the essential aspect of shape selective catalysis of molecular sieve catalysts. Elucidating the diffusion mechanism of molecules in the confined space of catalysts is of great importance for the efficient utilization of the porous materials in the catalytic reaction as well as the strategy proposal of reaction control in shape-selective catalysis. However, it is still a great challenge to understand and quantify the diffusion behavior at the molecular level for the establishment of the diffusion mechanism within the crystal of microporous materials as so far. In this work, with advanced pulsed field gradient (PFG) NMR technique, self-diffusion coefficients of alkanes (methane, ethane and propane) in three cavity-type molecular sieves (LEV, CHA and RHO) with very close eight-membered ring (8-MR) windows were determined. Furthermore, molecular dynamics (MD) simulations predicted the energy barrier for crossing 8-MR to be overcome. Based on MD simulations and a continuous-time random-walk (CTRW) method, not only the diffusion trajectory of the molecule can be visually displayed, but also the diffusion behavior is quantitatively described as the inter-cavity hopping process with the success extraction of the jump frequency (f) and jump length (L). The substantial role played by cavity structure and dimension in diffusion within cavity-type molecular sieves with the close 8-MR windows were revealed in depth, which would help to reveal the mechanism of cavity-controlled diffusion and propose the shape-selective strategy in the methanol-to-olefins process.

© 2019 Elsevier Inc. All rights reserved.

1. Introduction

The well-defined pores, the high crystallinity and the tuneable acidity have stimulated the growing attention in utilizing zeolite and zeotype materials in chemical industry, especially for catalysis and gas separation [1,2]. For these processes, understanding the confinement effect imposed by zeolite topology on the guest species is the key issue for shape-selectivity of adsorption, diffusion and reaction on the microporous materials, which is also of great

significance for understanding the mechanisms of catalytic reactions and separation processes [3–5].

The significance of the shape-selectivity and the confinement effect in the catalysis of zeolite and zeotype materials has been substantially confirmed in the methanol-to-olefins (MTO) reaction, the most successful catalytic process for the light olefins production via non-petrochemical routes from abundant resources of natural gas or coal [6–10]. The application of shape-selective catalyst with cavity structure and eight-membered ring (8-MR) channel, such as H-SAPO-34 with CHA topology in the MTO reaction, gives rise to highly-selective production of ethene and propene and also makes H-SAPO-34 an excellent commercial MTO catalyst. Besides H-SAPO-34, other 8-MR and cavity-type molecular sieves have been also proved to be shape-selective catalysts, and interestingly,

* Corresponding authors.

E-mail addresses: xushutao@dicp.ac.cn (S. Xu), zhenganm@wipm.ac.cn (A. Zheng), weiyx@dicp.ac.cn (Y. Wei), liuzm@dicp.ac.cn (Z. Liu).

¹ Both authors contributed equally to this work.

the unique product selectivity differs with the cavity type of the catalyst [10–13].

For the MTO reaction conducted over 8-MR and cavity-type catalysts, on one hand, the cavity geometry of these molecular sieves controls the accommodation and stabilization of the confined critical intermediates of the hydrocarbon pool (HP) mechanism [10,14–20], which varies the predominant route of olefin products generation during the efficient reaction stage and catalyst deactivation stage [9–11,13,21]. On the other hand, for the heterogeneous reaction catalyzed by aluminosilicates (zeolites) or silicoaluminophosphates (SAPOs), the topology of the catalyst, including the structure and dimension of the channel and cavity, also greatly influences the mass transport of reactants and products inside the catalysts due to that the reactants need to diffuse into the catalysts and contact with active sites and generated hydrocarbons need to diffuse out of the catalysts as effluent products. 8-MR and cavity structure of zeolites or SAPO molecular sieves work as the diffusion path or micro-reactor for mass transport and reaction. The narrow and restricted 8-MR pore openings of cavity-type molecular sieves limit the diffusion of higher hydrocarbon products, leading to extremely high selectivity toward lower olefins in the MTO process. As a result, for the important MTO process catalyzed by zeolites or SAPOs, the issue of guest molecular diffusion within confined surroundings goes beyond the configuration diffusion from the point of mass transfer, and plays a significant role in the achievement of high reaction activity for reactant conversion and selective generation of the products [22–26]. The strategy proposal for reaction control, the most critical issue of the important catalytic applications, requires the complete comprehension combining the understanding of the reaction and the diffusion of the reactant and product molecules in these catalysts. The detailed study presented the shape selectivity for ethene, propene and butene production can be varied with the usage of 8-MR SAPO materials with different cavity type [10], and revealed a special cavity-controlled intermediates formation and reaction in the cavity-type catalytic environments [9,10]. The catalysis and shape selectivity have been interpreted successfully based on the intensive efforts on the reaction mechanism [9,10], while the knowledge concerning the diffusion behavior in the catalysts of the practical industry process have been still highly desirable in this field.

Aiming at the deeper insights of confinement effect imposed by 8-MR and cavity-type catalysts on the diffusion of guest hydrocarbons, three cavity-type molecular sieves with very close 8-MR windows and different cavities (SAPO-35 with LEV, SAPO-34 with CHA and DNL-6 with RHO topologies) are elaborately selected, which are expected to present the diffusion behavior in the cavity-type catalysts. The intracrystalline diffusion of guest molecule within 8-MR and cavity-type molecular sieves has been depicted as an inter-cavity hopping process, which is a rare event that requires overcoming the diffusion restriction to pass through the 8-MR windows as revealed by computational studies [27–30]. It has been noticed that the narrow 8-MR pore openings of zeolites or SAPOs impose very strong steric hindrance for the inter-cavity hopping [27,29–31], while the whole chemical environments for guest molecular diffusion, originated from the cavity structure of the molecular sieve has not been interpreted in depth. Revealing the host-guest interactions along the intracrystalline diffusion path and quantifying the confinement effect of the chemical environments with 8-MR and different cavity structure on diffusion behavior would give deep insights of the diffusion mechanism and help to propose the shape selective strategy for relative catalytic reactions.

In this work, we intensively studied the diffusion of hydrocarbon molecules (methane, ethane and propane as the probe molecules) in the confined surroundings of 8-MR and cavity-type

SAPO molecular sieves. The applications of spectroscopic approaches [32,33] and theoretical simulations [5,34] for diffusion measurements enable fundamental studies of mass transport in confined environments and give more useful insights into the effect of zeolite topology on diffusion from a microscopic point of view. Pulsed field gradient (PFG) NMR, a well-suited tool for probing the diffusion in porous media [32,35,36], and molecular dynamics (MD) used for the microscopic description of diffusion mechanism inside microporous materials [5,24,37], have been employed to reveal that how the cavity structure controls the molecular diffusion through almost identical 8-MR windows. Complementary and reciprocal results based on the applications of the powerful tools present a very special cavity-controlled diffusion in the cavity-type molecular sieves with 8-MR windows, with the correlation of the diffusion of guest molecules to established cavity-controlled intermediates formation and reaction during the MTO process [9,10], an overall cavity-controlled shape selective reaction system could be constructed (Scheme 1). On one hand, cavity structure controls the accommodation and stabilization of the confined critical intermediates (see Scheme 1b) and the reaction routes of olefins formation [9,10]. Larger cavity structure (CHA and RHO) favors the formation of bulky-sized heptamethylbenzenium and pentamethylcyclopentadienyl cations as the most important intermediates, while the spatial restriction imposed by the smaller cavity (LEV) contributes to the generation of small-sized intermediates (tetramethylbenzenium and trimethylcyclopentadienyl cations) [9,10]. On the other hand, cavity structure and dimension control the molecular diffusion, especially the reactant diffusion, in turn could significantly influence the reactivity of hydrocarbons (see Scheme 1a). RHO with large-sized *lta* cavity greatly benefits the mass transport, while LEV with small cavity structure imposes stronger diffusion restriction for hydrocarbons. Therefore, both the confinement effect and diffusional restriction imposed by cavity structure contribute to the generation of desirable products, resulting in different MTO activity and product selectivity (see Scheme 1c) [10]. RHO exhibits the highest activity and butene is the predominant product, while LEV presents the lowest methanol conversion and ethene is the main product. Ethene and propene are formed as the main products in CHA. The cavity-controlled diffusion, critical intermediates formation and product generation explicitly present shape selectivity in the methanol-to-olefins process by the usage of different 8-MR and cavity-type catalysts based on host-guest interactions. The complete comprehension of the reaction mechanism and the diffusion of the reactant and product molecules in these catalysts would guide the proposal of reaction control for shape-selective catalysis.

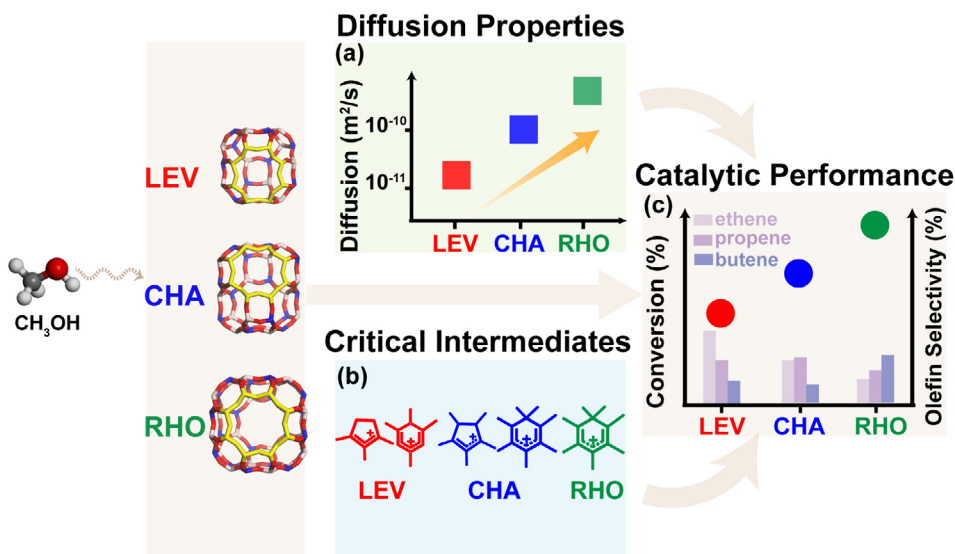
2. Experimental and computational methods

2.1. Experimental methods

2.1.1. Sample preparation

The SAPO molecular sieves (SAPO-35, SAPO-34 and DNL-6) were synthesized as reported in the literature [38–40]. Detailed procedures were performed as follows. SAPO-35 was synthesized from a mixture gel composition of 1.5 hexamethylenimine (HMI): 1.0 Al₂O₃:1 P₂O₅:0.8 SiO₂:55 H₂O. Typically, pseudo-boehmite (67.5 wt%), orthophosphoric acid (85 wt%), silica sol (30 wt%), deionized water and HMI were added into a glass beaker in a sequence and the mixture was stirred to form homogeneous gel. Then the initial gel was transferred into a stainless steel autoclave and heated at 200 °C for 24 h under rotation. SAPO-34 was hydrothermally synthesized from the gel ratio of 2.0 morpholine (Mor): 1.0 Al₂O₃:1.0 P₂O₅:0.6 SiO₂:60 H₂O. The mixture of

An overall cavity-controlled methanol-to-olefins reaction



Scheme 1. Shape selectivity in the methanol-to-olefins process: cavity-controlled diffusion (a), critical intermediates formation (b, tetramethylbenzenium and trimethylcyclopentadienyl cations in LEV; heptmethylbenzenium and pentamethylcyclopentadienyl cations in CHA and heptmethylbenzenium cations in RHO) [9] and product generation (c, ethene, ethene and propene, butene are predominant products in LEV, CHA and RHO, respectively) [10] in the MTO process over cavity-type molecular sieves with 8-MR windows.

pseudo-boehmite (67.5 wt%), orthophosphoric acid (85 wt%) and deionized water were stirred for 1 h to form homogeneous aqueous. Then silica sol (30 wt%) and morpholine were added dropwise into the aqueous. The resulting gel was aged under vigorous stirring for 12 h at room temperature, then transferred into stainless steel autoclave and heated at 200 °C for 48 h under rotation. The gel ratio for the synthesis of DNL-6 is: 5.0 N,N'-dimethylethylene diamine:1.7 Al₂O₃:1.0 P₂O₅:1 SiO₂:167 H₂O prepared by the mixture of aluminum isopropoxide, orthophosphoric acid (85 wt%), tetraethyl orthosilicate and deionized water. After addition of organic template agent N,N'-dimethylethylenediamine, the final mixture was transferred into stainless steel autoclave, which was heated at 200 °C for 12 h under rotation. All as-synthesized products were washed with distilled water and dried at 120 °C. The three samples were calcined at 600 °C for 4 h to remove the organic template, respectively.

2.1.2. Characterization

The powder X-ray diffraction (XRD) patterns were recorded on a PANalytical X'Pert PRO X-ray diffractometer with Cu K α radiation ($\lambda = 1.5418 \text{ \AA}$), operating at 40 kV and 40 mA. The morphology of crystals was obtained using field emission scanning electron microscopy (Hitachi SU8020). The chemical compositions were determined by X-ray fluorescence (XRF) spectrometer (Philips Magix-601). Nitrogen adsorption-desorption experiments were measured at 77 K on Micromeritics ASAP 2020.

2.1.3. Adsorbates

Methane, ethane and propane, which are similar to methanol, ethene and propene in molecular size, respectively, are chosen to probe the vital role of cavity structure in mass transport solely due to the small alkene oligomerization easily occurs on acid form zeolites at room temperature [41,42].

2.1.4. Pulsed-field gradient (PFG) NMR

Prior to PFG NMR experiments, all calcined samples were activated at 673 K for 12 h on a vacuum system to completely remove

volatile matter adsorbed in pore space. Subsequently a known amount of materials were transferred into the bottom of NMR tubes with 5 mm outer diameter (Wilmad-LabGlass) filled with a sealed quartz tube (diameter of ca. 3 mm) (see Scheme S1) in glove box. The required adsorbate was introduced quantitatively into the NMR tube on a homemade uptake apparatus, and the tubes were sealed off. The change of pressure sensor represents the amount of adsorbate in the samples. The loading of adsorbed molecules was calculated by the ideal gas equation. All data were acquired at equilibrium condition.

¹H PFG NMR experiments were performed on a Bruker Avance III 600 spectrometer equipped with a 5 mm diff50 diffusion probe, which provides the maximum gradient strength of 1800 G/cm in the z-direction. A bipolar-gradient stimulated echo sequence (STEBP, also called 13-interval sequence) [43] was applied in diffusion measurements to eliminate the effect of magnetic susceptibility in the beds of porous materials. STEBP sequence is also less susceptible to background effects which arises from probe and interferes with the NMR signal than STE or STE-LED (See Figs. S1–S2).

Typically, in the case of isotropic diffusion, self-diffusion coefficient D can be obtained by

$$I = I_0 \exp \left[-(\gamma \delta g)^2 D \left(\Delta - \frac{\delta}{3} \right) \right] \quad (1)$$

where I and I_0 is the signal amplitudes with and without g , respectively. γ is the gyromagnetic ratio of the ¹H nucleus, δ is the effective gradient pulse duration, g is gradient strength, Δ is the diffusion time. Optimal parameters (δ , Δ and g) were set for each sample in the PFG NMR measurements, respectively. The echo signals decayed exponentially with linearly increasing gradient strength while diffusion time and gradient pulse duration kept constant.

For a two-dimensional anisotropic system [44,45], the NMR echo attenuation can be described by

$$M(b) = M(0) \exp(-bD) \int_0^1 \exp(bDx^2) dx \quad (2)$$

where $b = (\gamma\delta g)^2 (\Delta - \frac{g}{3})$, the integral equation is expressed as follows:

$$M(b) = M(0) \frac{\sqrt{\pi}}{2} \exp(-bD) \frac{\operatorname{erfi}(\sqrt{bD})}{\sqrt{bD}} \quad (3)$$

where erfi represents the imaginary error function [44] used to mathematical analysis by MATLAB and obtain the self-diffusion coefficients.

2.2. Computational methods

2.2.1. Molecular dynamics simulation

In the simulations, the rigid Al-P version of LEV, CHA and RHO topologies was used. The initial framework structures of pure silicon were taken from the International Zeolite Associations database [46], then subsequently were substituted by Al and P atoms, and optimized by GULP [47] with SLC core-shell force field [48]. The Vdw force field parameters are assigned to ε/k_B ($\text{CH}_4\text{-CH}_4$) = 147.9 [K], σ ($\text{CH}_4\text{-CH}_4$) = 3.73 [Å] and ε/k_B ($\text{CH}_4\text{-O}_{\text{zeo}}$) = 160.9 [K], σ ($\text{CH}_4\text{-O}_{\text{zeo}}$) = 3.218 [Å]. The selected super cells are $3 \times 3 \times 2$, $3 \times 3 \times 3$ and $3 \times 3 \times 3$ for LEV, CHA and RHO, respectively. These cell parameters were used in the molecular dynamics (MD) simulation. The NVT ensemble, where the number of particles (N), volume (V) and temperature (T) keep constant, was used in all the MD simulations. The simulated temperature was held at 298 K and controlled by a Nosé-Hoover thermostat with a coupling time constant of 1 ps. The velocity Verlet algorithm was used to integrate the Newton's equations of motion with a time step of 1 fs. The Lennard-Jones interactions were calculated with a 12 Å cutoff radius and periodic boundary conditions were also used in all three directions. Each MD simulation was equilibrated for 2 ns, then following 100 ns production for studying the diffusion behavior of methane molecules. The trajectories were recorded every 1000 steps and five independent MD simulations were carried out for better statistics. The fluctuations of the temperature and the stability of conserved quantity throughout the simulation were checked (see Figs. S3 and S4). The parameters of force field were given in the original reference by Sholl [49]. All MD simulations were performed in the parallel general purpose DL_POLY_2.20 code [50].

2.2.2. Calculation of pore diameters

Using the previous features of the identification of rings, ring diameters have been implemented by calculating the distance between two opposite oxygen atoms and subtracting twice the IZA-recommended value of the oxygen radius (1.35 Å) [51,52]. The minimum and maximum diameters of 8-MR window were recorded, respectively.

2.2.3. Diffusion coefficient

The mean square displacement (MSD) of an adsorbed molecule is defined as the following equation:

$$\text{MSD}(\tau) = \frac{1}{N_m} \sum_i^{N_m} \frac{1}{N_\tau} \sum_{t_0}^{N_\tau} [r_i(t_0 + \tau) - r_i(t_0)]^2 \quad (4)$$

where N_m is the number of adsorbed molecules, N_τ is the number of time origins used in calculating the average, and r_i is the coordinate of the center of mass of molecule i . The slope of the MSD as a function of time determines the self-diffusion coefficient, D_s , defined according to the so-called Einstein relation [53].

$$\text{MSD}(\tau) = 2nD_s\tau + b \quad (5)$$

where n is the dimension of frameworks ($n = 2, 3$ and 3 for LEV, CHA and RHO, respectively), b is the thermal factor arising from atomic

vibrations. The diffusion coefficients were obtained by fitting the MSD against time in the region of 1000–10,000 ps (linear region) using a least-square fit. The reported MSD curves and corresponding D_s values were calculated as the average of five independent MD trajectories.

2.2.4. Interaction energy

Firstly, a methane molecule was placed into the center of one cavity, and then systematically moved to another center of the adjacent cavity following the diffusion path with 50 equi-spaced steps. The interaction energy between framework and molecule at each point was calculated and the energy barrier for crossing 8-MR was determined by the difference between the lowest and highest energy along the diffusion pathway [54].

2.2.5. Diffusion radius

The diffusion radius of methane molecules can be extracted from diffusion trajectory in three cavity-type molecular sieves, respectively. The diffusion radius R is given by

$$R = \frac{1}{N} \sum_{i=1}^N \max\{r_i(t_1 \rightarrow O_i), r_i(t_2 \rightarrow O_i), r_i(t_3 \rightarrow O_i) \cdots r_i(t_{\text{tot}} \rightarrow O_i)\} \quad (6)$$

where N is the number of adsorbed methane molecules, O_i is the center of the i -st methane trajectory and r_i is the distance between methane (at any time t) and the center. Here, R represents the average diffusion radius of methane molecules. Firstly, the trajectory of each methane was picked up and corresponding center was recorded as position O_i . Then the distance between O_i and each point in the trajectory was calculated. After that, the diffusion radius of the i -st methane is recorded as the longest distance among these trajectories. Finally, the averaged radius of methane molecule is recorded as R .

2.2.6. Monte Carlo simulation

Monte Carlo (MC) simulations were also performed in the canonical ensemble (NVT). The parameters of force field are the same as above molecular dynamics methods. The MC simulations proceed for 100,000 cycles of equilibration followed by 100,000 of production. The structure was printed every 100 cycles after equilibration to analyse the density maps. During Monte Carlo simulations, move types of translation, rotation, reinsertion and swap with probabilities of 25%, 25%, 25% and 25% were used, respectively. The simulations were performed by RASPA 2.0 simulation package [55]. The density maps were shown by VTK software (<http://www.vtk.org>).

2.2.7. A continuous-time random-walk (CTRW) coarse graining method [56]

In coarse-graining time algorithm, the center of the k -th dynamic basin of the tagged methane molecule, $\bar{R}(n)_k$, is done iteratively as

$$\bar{R}(n)_k = \frac{(n-1)\bar{R}(n-1)_k + R(n)}{n} \quad (7)$$

The average is updated until $R(n+1)$ walks out of a certain range:

$$\left\{ \begin{array}{l} \leq D_{\text{max}} \text{ update the basin center position} \\ > D_{\text{max}} \text{ start the new basin} \end{array} \right\} \quad (8)$$

D_{max} was set to 8, 8 and 13 Å, respectively, which was found to be a reasonable value for the methane, as a threshold of the basin crossing in LEV, CHA and RHO, respectively. The past n snapshots are

defined as a dynamical basin centered at $\bar{R}(n)_k$. If the labelled molecule hops into a new basin according to Eq. (8), the running index n is updated to 1. The hopping time τ is defined as the average waiting time of methane within dynamic basin, while the jump length L is the average distance between two consecutive basin centers $\langle \bar{R}_{k+1} - \bar{R}_k \rangle$.

3. Results and discussion

3.1. SAPO-35 with LEV, SAPO-34 with CHA and DNL-6 with RHO topologies

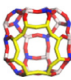
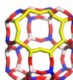
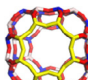
Configurational features of cavity-type molecular sieves with LEV, CHA and RHO topologies, respectively, are shown in Table 1. These topologies have different cavities connected via similar 8-MR windows. The cavity size of the selected 8-MR molecular sieves varies in topology and differs in dimension with an increased order of LEV < CHA < RHO. SAPO-35, SAPO-34 and DNL-6 are expressed as LEV, CHA and RHO in following text, respectively.

Powder X-ray diffraction (XRD) patterns and scanning electron microscopy (SEM) clearly demonstrate the high-crystallinity and pure-phase of SAPO molecular sieves (see Figs. S5–S6 in the Supporting Information, SI), respectively. SAPO-35 (LEV) presents diamond-shaped particles with crystallite size of 12 μm . SAPO-34 (CHA) is typical cuboid crystal in the range of 10–15 μm , and DNL-6 (RHO) with a particle size of 10 μm exhibits rhombic dodecahedral morphology. The large size of the crystals of SAPO-35, SAPO-34 and DNL-6 ensures that molecules remain in the intracrystalline space during the whole diffusion time of PFG NMR measurements to obtain the intracrystalline diffusion coefficients without the influence of shape and dimension of crystals under this study. Table S1 summarizes the chemical compositions and textural properties of SAPO molecular sieves. These characterizations confirmed the crystallinity and purity of the selected molecular sieves and allowed the appropriate comparability to reveal the impact of topology alone on the molecular diffusivities.

3.2. Diffusion characteristics of methane in cavity-type molecular sieves

Three SAPO molecular sieves with methane were prepared (see Experimental methods). Methane was selected as a model probe to quantitatively reflect the molecular diffusion due to its small size (kinetic diameter 3.8 Å) and stability. The typical ^1H PFG NMR spectra of methane adsorbed in cavity-type molecular sieves (LEV, CHA and RHO) measured at 298 K as gradient strength (g) linearly increases were presented in Fig. 1(a)–(c), respectively. The corresponding ^1H PFG NMR spin echo attenuation decays as a function of $\delta^2\gamma^2g^2(\Delta - \delta/3)$ on a log-linear scale (Fig. 1d–f) for methane in cavity-type molecular sieves, respectively. In the case of CHA and RHO with three-dimensional channels, the linear fittings of semi-logarithmic plots for the attenuation of I/I_0 (Fig. 1e,f) were presented using the Stejskal-Tanner (Eq. (1)) for standard three-dimensional isotropic diffusion [32,45]. For LEV, a nonlinear variation in semi-logarithmic plot of echo attenuation with $\delta^2\gamma^2g^2(-\Delta - \delta/3)$ on the log-linear scale was presented and Eq. (1) cannot fully fit the PFG NMR data (black line in Fig. 1d). In the case of LEV, molecular motions only occur along the [1 0 0] and [0 1 0] directions. While along [0 0 1] direction, extremely narrow pore size of 6-membered ring (6-MR) that is significantly smaller than kinetic diameter of methane limits the diffusion of methane. Therefore the anisotropic diffusion in LEV with two-dimensional channels is to be expected [45]. For such a two-dimensional anisotropic system, as shown in Fig. 1d, the PFG NMR spin echo attenu-

Table 1
Configurational properties of cavity-type molecular sieves.

	LEV	CHA	RHO
Topology			
Molecular sieves	SAPO-35	SAPO-34	DNL-6
Cavity dimension/Å ²	8.1 × 9.4	9.1 × 10.8	11.4 × 11.4
Window size ^a /Å ²	3.2 × 4.9	3.5 × 4.4	4.0 × 4.3
Cavity density ^b /10 ⁻³ Å ⁻³	1.69	1.21	0.59

^a The minimum and maximum diameters of the 8-MR and the calculation details in the Computational methods.

^b The number of cavities per 1000 Å³ in framework.

ation could be well fitted by Eq. (2) (see details in the Experimental methods) on the log-linear scale (the orange fitting line, Fig. 1d) [44,45].

The self-diffusion coefficients, D , of methane within cavity-type molecular sieves were extracted from PFG NMR echo attenuation and presented in Fig. 1(g)–(i). A general comparison indicates that self-diffusion coefficient of methane in RHO molecular sieve (5.4×10^{-10} m²/s) is notably higher than that in both CHA (1.2×10^{-10} m²/s) and LEV (2.7×10^{-11} m²/s) with two methane molecules per cavity measured at 298 K in Fig. 1g. For LEV, self-diffusion coefficient of methane exhibits a minimum value of 2.7×10^{-11} m²/s among the three cavity-type molecular sieves. As shown in Table 1, an increase in self-diffusion coefficient of methane inside cavity-type molecular sieves is clearly presented with cavity dimension at the identical loading.

Furthermore, the self-diffusion coefficient is closely related to the molecular concentration [29,57,58]. The loading dependence of the self-diffusivities is strongly determined by pore properties of zeolite (i.e., pore size, pore shape and pore type), and thus the different loading-dependent diffusion coefficients have been confirmed in the previous work [29,57–59]. The loading dependence of self-diffusion coefficients for cavity-type molecular sieves was presented in Fig. 1h. In the case of LEV, a remarkable enhancement about one order of magnitude in self-diffusion coefficient of methane was displayed as loading increased from 0.4 to 2.1 molecules per cavity. And for CHA, the increase of self-diffusion coefficient about 43% took place at loading in the range of 0.7–2.2 molecules per cavity. However, for RHO, self-diffusion coefficient of methane exhibited the least sensitive with increasing loading from 0.9 to 3.1 molecules per cavity. This loading dependence clearly shows that the effect of loading on self-diffusion coefficient is strongly dependent on the cavity dimension of the 8-MR and cavity-type molecular sieves and the smaller the cavity is, the bigger variation in self-diffusion coefficient is, which is closely correlated with the confinement imposed by cavity structure [58]. Moreover, for the methane loading in range of 0.5–2 molecules per cavity, self-diffusion coefficient of methane always follows the order of RHO > CHA > LEV, although the diffusion coefficients change as the loading increases. Therefore, it is indicated that such a reduction in diffusion within cavity-type molecular sieves can be ascribed to the enhanced restriction or confinement from the environments with cavity structure for the molecular diffusion from RHO to LEV.

To further verify the aforementioned results, molecular dynamics (MD) simulations was used to evaluate the effect of zeolite topology on diffusion, which has contributed to obtain deep insights into diffusion mechanism [5]. Since methane is a stable and symmetric sphere molecule, and the weak interaction between methane with acid site is presented when methane diffuses in the pores [60], AIPO structure was selected as a model to quantita-

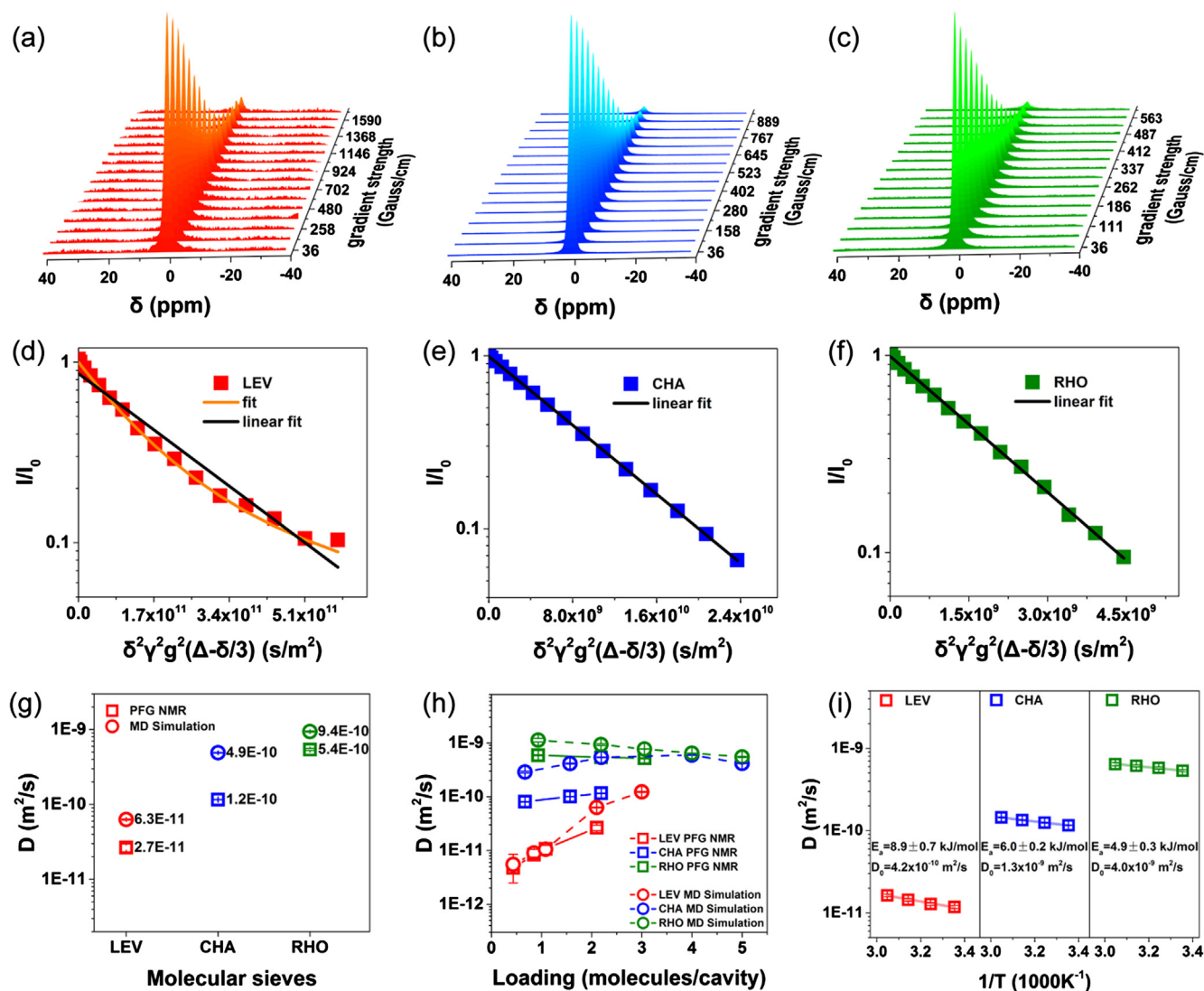


Fig. 1. Diffusion characteristics of methane in cavity-type molecular sieves. (a–c) ^1H PFG NMR signals decay with linearly increasing gradient magnetic field strength in 16 steps for LEV (a), CHA (b) and RHO (c) measured at 298 K. (d–f) The corresponding spin echo attenuation of PFG NMR as a function of $\delta^2\gamma^2g^2(\Delta - \delta/3)$ on the log-linear scale for LEV (d), CHA (e) and RHO (f). The black lines are linear fittings for isotropic diffusion and the orange line is the fitting curve for two-dimensional anisotropic diffusion in LEV. (g) The experimental (PFG NMR) and simulated (MD) self-diffusion coefficients of methane in LEV, CHA and RHO at the loading of two molecules per cavity at 298 K. (h) The loading dependence of experimental and simulated self-diffusion coefficients for methane in cavity-type molecular sieves at 298 K. (i) The temperature dependence of self-diffusion coefficients on the log-linear scale for methane within cavity-type molecular sieves in the temperature range of 298–328 K and corresponding diffusion activation energies (E_a) as well as pre-exponential factors (D_0) calculated by Arrhenius law. Open square and open circle represent experimental and simulated values, respectively. Error bars are marked on all the symbols. The error bars are based on the standard errors for PFG NMR and MD simulations.

tively reflect the substantial role of cavity structure in molecular diffusion behavior. From the slope of mean square displacement (MSD) curves (see Fig. S7 in the SI), the self-diffusion coefficients of methane in aluminophosphates (ALPOs) with LEV, CHA, and RHO topologies loaded with different loadings at 298 K, respectively, was determined and displayed in Fig. 1h. As seen from PFG NMR data and MD simulations, a consistent variation is noted between the experimental and theoretical values of diffusion with the increase of methane loading for three microporous materials, respectively. Importantly, the diffusion in different materials obtained by MD simulations leads to the conclusion that the diffusion rate increases with an order of $\text{RHO} > \text{CHA} > \text{LEV}$ in the range of loading studied, which is well coincident with PFG NMR results. It should be noted that the higher diffusion coefficient by MD simulation compared to that by PFG-NMR may be attributed to the absence of acid sites.

Moreover, the self-diffusion coefficients of methane within cavity-type molecular sieves in the temperature range of 298–

328 K were measured by PFG NMR experiments and plotted in Fig. 1i, loaded with two methane molecules per cavity. The apparent diffusion activation energies (E_a) and pre-exponential factors (D_0) were calculated for methane on the basis of the Arrhenius law [61]:

$$D = D_0 \exp(-E_a/RT) \quad (9)$$

The apparent activation energy corresponds to the barrier that the diffusion of methane molecule needs to overcome on diffusion pathways within molecular sieves [61]. When the three cavity-type molecular sieves were evaluated, the calculated diffusion activation energies also vary with the molecular sieve used. Diffusion activation energies, E_a , exhibit a maximum (8.9 kJ/mol) for LEV and a minimum (4.9 kJ/mol) for RHO. At the same time, the pre-exponential factor, D_0 , representing the diffusivity at infinitely high temperature, is highly related to the geometrical restriction of

guest molecules within the molecular sieves [61]. For methane in RHO, the lowest value of activation energy together with the highest pre-exponential factor corresponds to the fastest methane diffusion. Comparatively, the highest activation energy and the lowest pre-exponential factor indicate the most dominant steric hindrance originates from cavity structure of LEV molecular sieve in intracrystalline diffusion process.

Although the diffusion is closely related to the loading and temperature, methane diffusion increases in the order of RHO > CHA > LEV. Given this consideration, in the following content, diffusion within the molecular sieves environments with the same 8-rings windows and varied cavity structure was evaluated by theoretical simulations in details from the view of cavity structure, including adsorption structure, interaction energy and diffusion trajectory as follows.

3.3. Adsorption structure

To disclose the molecular diffusion mechanism in cavity-type molecular sieves, firstly, the adsorption structures of methane in these molecular sieves were investigated theoretically. Monte Carlo (MC) simulation is a reliable method to predict the distribution of gas molecules inside porous materials [5]. Density maps have been used to present the preferred adsorption sites within pores, which can comprehensively rationalize the diffusion process at the molecular level [62,63]. The map for methane adsorption is drawn as 3D histogram with red density plot, and the surface of material is depicted with a blue-white volume rendering method. For LEV topology, it is observed that most methane molecules are densely adsorbed at the top and bottom of cavity (Fig. 2b) and near the center of six-membered ring

(6-MR) but not close to 8-MR (Fig. 2a), which means that methane prefer to stay in the center of *lev* cage. While for CHA topology, the most stable adsorption site is located at the outer edge of *cha* cavity which is close to the 8-MR windows, as shown in Fig. 2(c) and (d). In the case of RHO topology, the density maps indicate that most favorable adsorption site for methane is the center of double 8-MR region (Fig. 2e and f). It should be noted that few methane molecules are concentrated at the center of the cavity and the presented red colour at the center is due to the overlapped projection from double 8-MR region, which is further illustrated in Fig. S8 in the SI. By the prediction of the distribution of methane inside cavity-type materials with 8-MR windows, the preferred adsorption sites that were attributed to structural features with different cavity shape and size could be identified. In subsequent section, an interaction between methane and framework was employed to give a more detailed understanding of the preferred adsorption sites and corresponding contribution to diffusion behavior.

3.4. Interaction energy

In order to understand the preferred adsorption sites and inter-cavity motions process for methane diffusion, the interaction energies profiles between the frameworks and adsorbed methane inside cavity-type molecular sieves is necessary. It is well known that energy profiles present the variation of host-guest interactions between molecular sieves and methane guest along the diffusion pathways at molecular level and predict the energy barrier for crossing 8-MR window, as the methane diffuses from one cavity to adjacent cavity [64,65].

The interaction energy calculation was performed with a methane molecule moving from the center of the one cage toward the center of the eight-membered ring window and finally to the center of the adjacent cage as diffusion path (See Fig. 3a–c). For LEV with two types windows (6-MR window and 8-MR window), the interaction energy was predicted along two pathways. As methane coordinate perpendicular to a 6-MR window, methane encounters the very high barrier (1130.2 kJ/mol) for crossing the 6-MR window of LEV, which indicates that methane cannot diffuse through the 6-MR (see Fig. S9 in the SI). For the pathway through the 8-MR window between adjacent cavities in LEV (Fig. 3a and 3d), the energy barrier is 23.9 kJ/mol. Therefore, methane diffusion is energetically favorable through the 8-MR windows in LEV during the inter-cavity motions. For CHA and RHO topologies, the diffusion pathways and energy profiles of methane along this pathway is shown in Fig. 3b, e and c, f, respectively.

Generally, low energy barrier for crossing 8-MR can effectively facilitate the inter-cavity motions. According to the energy profiles, among the three concerned topologies, LEV exhibits the highest barrier of 23.9 kJ/mol for inter-cavity motions of methane, corresponding to the lowest value of diffusion coefficient. The energy barrier value (12.6 kJ/mol) in RHO for inter-cavity motions is higher than that of CHA (6.7 kJ/mol), however, methane diffusion in RHO is faster than that in CHA as measured in PFG NMR experiments and MD stimulations. Thus, it is indicated that the energy barrier for crossing 8-MR in the inter-cavity motions is not the only factor to control the methane diffusion inside cavity-type molecular sieves. Together with the feasibility of jump for inter-cavity diffusion determined by energy barrier for crossing 8-MR, the length of each inter-cavity jump, which is closely related to the dimension and structure of the cavity, also may play a crucial role in the diffusion behavior. Therefore, further exploration for more comprehensive diffusion characters was conducted at microscopic level by the introduction of the molecular dynamics (MD) simulations.

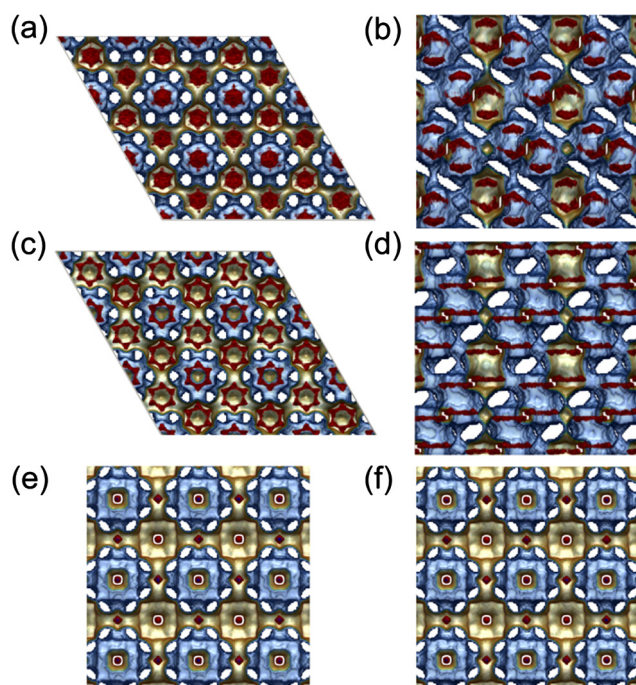


Fig. 2. Density maps for methane in three cavity structures obtained from Monte Carlo simulations with two molecules per cavity at 298 K. (a,b) The $3 \times 3 \times 2$ supercell crystal structure of LEV are viewed along [001] (a) and [010] (b) directions. (c,d) The $3 \times 3 \times 3$ supercell crystal structure of CHA are viewed along [001] (c) and [010] (d) directions. (e,f) The $3 \times 3 \times 3$ supercell crystal structure of RHO are viewed along [001] (e) and [010] (f) directions. The material surfaces (blue-white volume rendering), channels (goldenrod color) and density maps (red) are drawn.

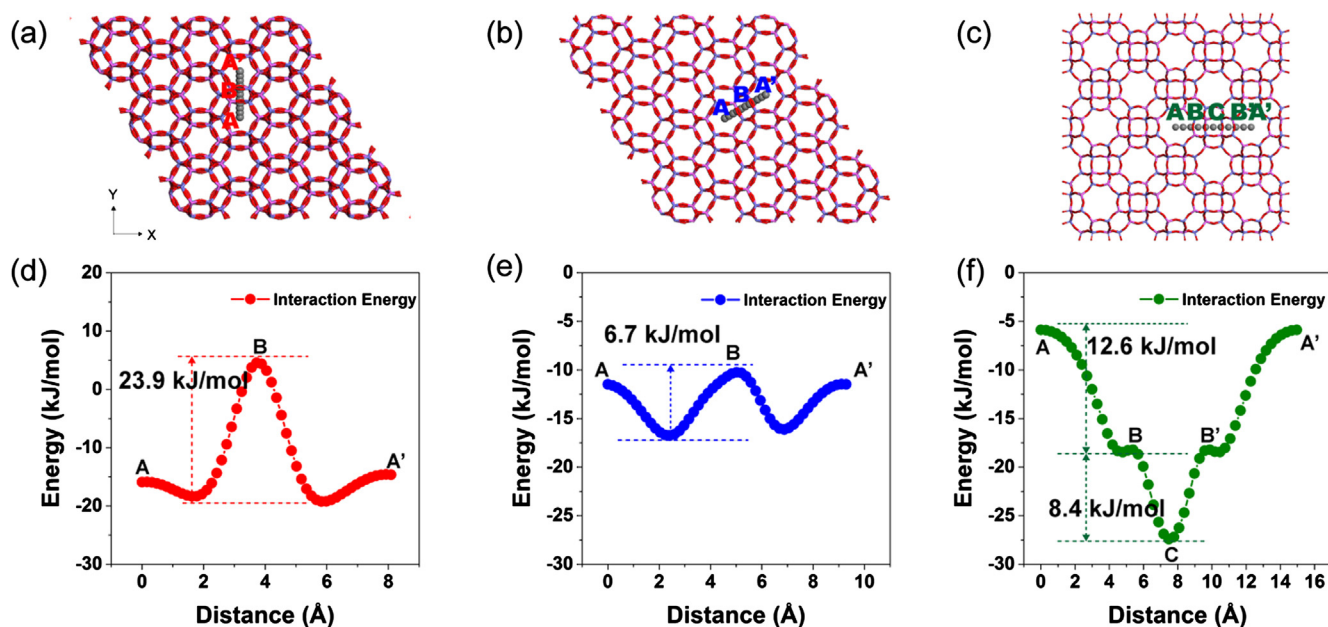


Fig. 3. Interaction energy profiles of methane in cavity-type molecular sieves. (a–c) Definition of diffusion pathways for the center of one cavity to the center of adjacent cavity through the 8-MR window in LEV (a), CHA (b), and RHO (c), respectively. (d–f) Energy profiles of methane as a function of the distance while methane is pulled from the center-of-mass of cavity (A) to the center-of-mass of adjacent cavity (A') in LEV (d), CHA (e) and RHO (f).

3.5. Diffusion trajectory

It is well known that the MD simulations can display the visualization of diffusion trajectory and provide detailed diffusion characters in microscopic view that are inaccessible in experiments and contribute to the understanding of diffusion mechanism [37,66].

Fig. 4(a)–(c) show the representative diffusion trajectories in XY plane (in $[0\ 0\ 1]$ direction) of LEV, CHA and RHO topologies, respectively, during diffusion time of 100 ns (two methane molecules per cavity for simulations). The diffusion radius R (which is defined in the Computational methods) of methane inside three cavity-type materials in certain time can be extracted from the corresponding diffusion trajectories and is presented in Fig. 4(a)–(c), respectively. In the identical diffusion time (100 ns), the diffusion distance follows the order of LEV (41 Å) < CHA (132 Å) < RHO (184 Å) in XY plane and the same trends are also observed in XZ and YZ planes, respectively (see Fig. S10 in the SI). The largest diffusion radius in RHO indicates that methane goes through the longest diffusion distance with the highest diffusion rate in this topology, which is also well consistent with the aforementioned self-diffusion coefficients derived from PFG NMR and MD results. Detailed analysis of methane diffusion trajectories clearly shows that methane diffuses by hopping process in these cavity-type molecular sieves with 8-MR windows. Preferential intra-cavity motions and occasional inter-cavity jumps through 8-MR window generate the diffusion trajectories at the time scale for methane diffusion in three molecular sieves. Such an inter-cavity hopping process, in which the methane jumps from one dynamic basin (e.g. cavity or adsorption site) to another dynamic basin, is a probabilistic event which is determined by the energy barrier for passing through the narrow 8-MR window between adjacent cavities. Therefore, the energy barrier of inter-cavity jump is very significant. The high barrier hinders the inter-cavity jump of methane through 8-MR windows, therefore LEV exhibits relatively lower number of inter-cavity jumps compared with CHA and RHO (see in Fig. 4a–c). Additionally, as shown in Fig. 4(a)–(c), each jump of guest molecule has to cover a certain distance to ensure that jump occurs from one dynamic basin to another dynamic basin for inter-cavity hopping process.

Among the three topologies, RHO with the largest cavity dimension exhibits the longest distance of jump between adjacent sites compared to that of LEV and CHA, which is also consistent with the results of varied adsorption structure of methane within the cavity-type molecular sieves (Fig. 2).

3.6. The continuous-time random-walk (CTRW) coarse-graining method

Based on the diffusion trajectory profiles for the cavity-type molecular sieves (Fig. 4a–c), here, the inter-cavity hopping process for the description of diffusion in 8-MR and cavity-type molecular sieves can be regarded as 'hurdle race', which is directly determined by jump frequency and jump length. High jump frequency and long jump length will lead to final success. Therefore, for the first time, a continuous-time random-walk (CTRW) coarse-graining method allowing for the determination of jump frequency and jump length based on molecular dynamics simulations [56,67], was introduced for quantitatively rationalizing diffusion characteristic inside the cavity-type molecular sieves. In this model, using a coarse-graining algorithm to identify dynamical basins, the single-molecule MD trajectory can be described by hopping time τ (or the jump frequency f) and jump length L (see Computational methods). The hopping time is defined as the average waiting time of methane within a dynamic basin for each jump, while the jump length is the average distance between two consecutive basin centers.

Fig. 4(d)–(f) show the three-dimensional coordinates (X, Y and Z) of methane in the inter-cavity hopping process as diffusion time increases based on the MD trajectories and the corresponding criterion of jump from the CTRW coarse-graining method in three cavity-type molecular sieves, respectively. For LEV topology, the diffusion trajectory of methane is only displayed in both X and Y directions as methane cannot diffuse through the 6-MR along Z direction, while diffusion trajectory of methane in CHA and RHO is three-dimensional with X, Y and Z directions, respectively (see Fig. 4d–f). Firstly, the validity of the CTRW coarse-graining method was confirmed for the application in the mass transport within cavity-type molecular sieves (see Computational methods). Briefly,

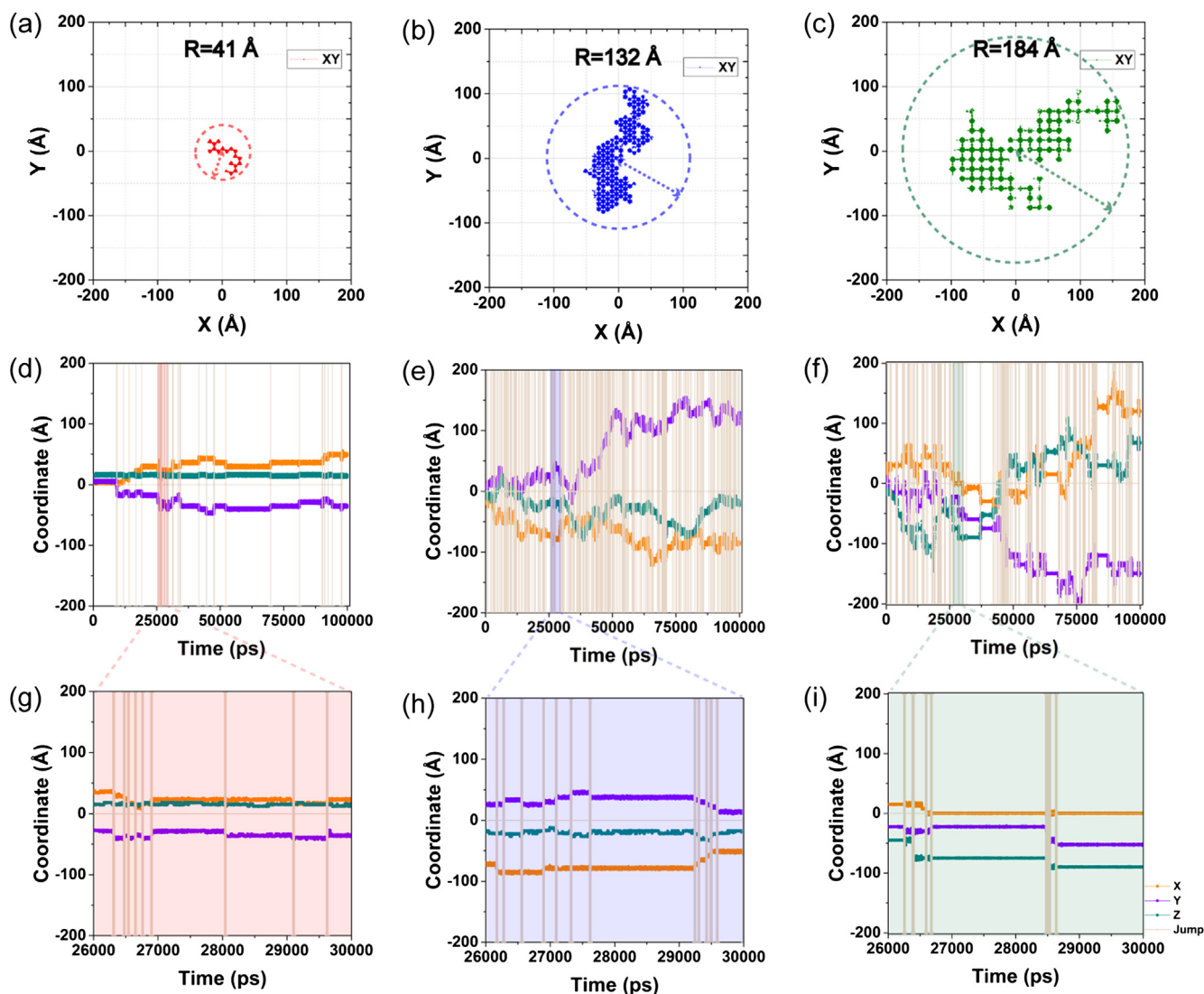


Fig. 4. Diffusion trajectories of methane inside cavity-type molecular sieves. (a–c) Trajectories of the one representative methane molecules diffusion in aluminophosphates LEV (a), CHA (b) and RHO (c) structure in XY plane at 298 K with loadings of two molecules per cavity and diffusion time of 100 ns, R represents the diffusion radius. (d–f) The coordinates of one representative methane in X (orange), Y (purple), Z (dark green) directions in the inter-cavity hopping process versus diffusion time and the corresponding the criterion of jump (cream-coloured) based on the CTRW coarse-graining method in LEV (d), CHA (e) and RHO (f), respectively. (g–i) Enlarged views (diffusion time of 26 to 30 ns) are shown as LEV (g), CHA (h) and RHO (i), respectively. The criterion of jump (cream-colored) refers to the occurrence of inter-cavity jump using the CTRW method.

for a methane molecule, its average position $\bar{R}(n)$ of dynamic basins (refers to a cavity) along the MD trajectory is calculated by averaging its center of mass. If the length between $\bar{R}(n)$ and $R(n+1)$ is larger than the set distance D_{\max} , it is assumed that inter-cavity jump has occurred between basin n to $n+1$ dynamic basins. For example, as depicted in Fig. 4d and g, the achievement of the jump of methane from one basin to another basin at 26300, 26,900 and 29,100 ps (represented cream-colored) in LEV derived from this algorithm is well corresponding to the diffusion behavior of methane in LEV based on MD trajectories (Fig. 4a). This is also confirmed in CHA (Fig. 4e and h) and RHO (Fig. 4f and i) topologies, respectively. Therefore, the MD trajectory of methane in cavity-type molecular sieves is successfully quantified using the CTRW method with the extraction of the jump frequency and jump length of inter-cavity hopping process, which provides the inherent property of mass transport in cavity-type molecular sieves with 8-MR windows.

As presented in Fig. 5, the jump frequencies of methane in LEV, CHA and RHO are 0.4, 3.3 and 2.8/ns, respectively. The extremely

low methane jump frequency shows that methane molecules prefer to stay in *lev* cavity for LEV. Comparing to LEV, the jump frequencies in RHO and CHA are 7 to 8 times higher than that in LEV, respectively. Combined with results of interaction energy, the energy barriers for crossing 8-MR window allow us to explain the difference in jump frequency in inter-cavity hopping process. The low barrier for crossing 8-MR window leads to the frequent occurrence of inter-cavity jumps, which thus shows a positive contribution to the higher jump frequency. In the case of three cavity-type molecular sieves, the highest barrier of 23.9 kJ/mol was determined in the inter-cavity jump for LEV, corresponding to the lowest jump frequency of methane, as presented in Fig. 5. Combining the variation of jump frequency to the energy barrier for crossing 8-MR of inter-cavity jump, it can be concluded that cavity structures of CHA and RHO energetically favor the inter-cavity jump through the 8-MR window, while small cavity structure of LEV depresses the inter-cavity motion. It is noteworthy that the dimension of pore is also as one of contributor to low jump frequency in LEV due to diffusion occurs only in XY plane (See Fig. S10). These results of dynamic simulation also were

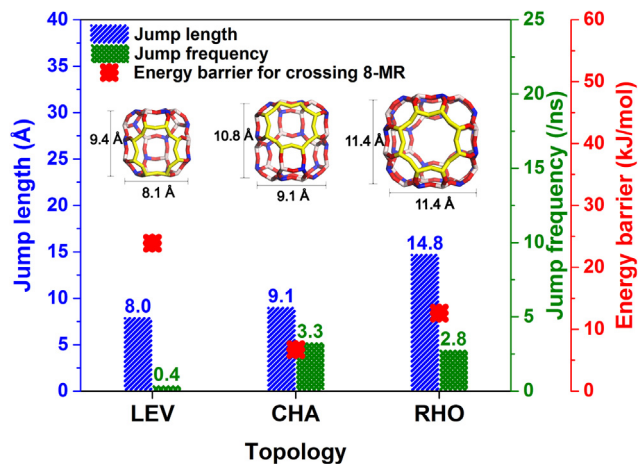


Fig. 5. The average jump frequency (f) and jump length (L) of methane in LEV, CHA and RHO extracted from diffusion trajectories via the CTRW coarse-graining method and the corresponding energy barrier for crossing 8-MR of methane in the inter-cavity hopping process.

checked (see Table S2) in 200 ns, which is in accord with that in 100 ns simulations.

It is noteworthy that besides jump frequency, the jump length also plays a crucial role in the inter-cavity hopping process as revealed by the MD trajectories in Fig. 4(a)–(c). Even the most frequent inter-cavity jumps of methane occur in CHA with the high jump frequency of 3.3/ns, compared with that in RHO (2.8/ns), while the highest mass transport rate of methane was measured in RHO. In the inter-cavity hopping process, although the jump frequency of methane in RHO is slightly lower than that in CHA, methane exhibits a longest jump length (14.8 Å) in RHO compared with that (9.1 Å) in CHA. As a result, for the inter-cavity hopping process, containing the jump frequency and the jump length of each jump, RHO conquers CHA in term of diffusion rate. The length of each jump between the adjacent sites in adjacent cavities (Fig. 4a–c) is closely related to the cavity dimension. As shown in Table 1, the cavity is sorted by size of LEV ($8.1 \times 9.4 \text{ \AA}^2$) < CHA ($9.1 \times 10.8 \text{ \AA}^2$) < RHO ($11.4 \times 11.4 \text{ \AA}^2$) and the cavity density, denoting the number of cavity per 1000 \AA^3 in framework, is contrary to the order of the cavity dimension (Table 1). In the present study, the inter-cavity hopping of large cavity structure presents long distance of each jump and the jump length follows the order of LEV (8.0 Å) < CHA (9.1 Å) < RHO (14.8 Å) with the increase of cavity dimension, corresponding to the decline in cavity density. Therefore, the variation in mass transport of methane within molecular sieves can be correlated to the cavity structure of the materials, which leads to the important conclusion of cavity-controlled diffusion. This conclusion is by no means limited to low temperature. Diffusion of methane within three cavity-type molecular sieves was also predicted at 673 K by MD simulation (see Fig. S11). A general comparison indicates that self-diffusion coefficient of methane also follows the order of RHO > CHA > LEV at 673 K although diffusion increases as temperature increases from 298 to 673 K. The jump frequency increases from 0.4/ns to 7.8/ns for LEV, from 3.3/ns to 22.4/ns for CHA and from 2.8/ns to 18.1/ns for RHO, respectively. Therefore, the increase in temperature facilitates the inter-cavity jumps, while the jump length almost kept constant which is close to the distance between two cages.

Furthermore, based on the CTRW method, the loading dependence of jump frequency and jump length for methane in cavity-type molecular sieves also is shown in Fig. S12. The jump lengths almost keep unchanged with loading for three molecular sieves, while jump frequencies change obviously which is main responsi-

Table 2

The self-diffusion coefficients of alkanes (methane, ethane and propane) in LEV, CHA and RHO measured at 298 K by PFG NMR^a

	D (CH ₄) m ² /s	D (C ₂ H ₆) m ² /s	D (C ₃ H ₈) m ² /s
LEV	2.7×10^{-11} (2)	–	–
CHA	1.2×10^{-10} (2)	6.0×10^{-12} (0.9)	–
RHO	5.4×10^{-10} (2)	1.4×10^{-10} (2)	5.4×10^{-13} (2)

^a The number in bracket is the loading per cavity.

ble for the variation of diffusion coefficient of methane with loading. The decreased jump frequency and jump length are responsible for the reduction in diffusion coefficient of methane with loading in RHO. In the case of CHA and LEV, an increased diffusivity with loading can be attributed to an increased jump frequency. At high loading, a small decrease in diffusivity for CHA is probably due to larger sorbate-sorbate repulsions as saturation is approached.

3.7. Diffusion characteristics of alkanes in cavity-type molecular sieves

To reveal the shape selectivity of the cavity type and 8-MR catalysts for the diffusion of molecules with different size, the intracrystalline diffusion was also probed by some other alkanes (ethane and propane) with relatively large molecular size (Table 2). The alkane diffusion in the same cavity-type molecular sieves varies with the guest molecular dimension and propane exhibits the lowest value of diffusion rate, indicating the increased diffusion restrictions. It is worthy to mention that, since the diffusion of propane in CHA, as well as ethane or propane in LEV encounter more severe diffusion restrictions than that in RHO, the extremely low diffusion coefficients cannot be measured by PFG NMR technique. The diffusion of ethane in CHA-type molecular sieves is in reasonable agreement with Dai et al. work [68]. The high diffusion rate of ethane and propane was presented in RHO compared to CHA and LEV. This indicates that RHO with relatively large-sized *lta* cavity greatly benefits the mass transport of guest molecules and small cavity structure imposes stronger diffusion restriction for larger hydrocarbons, which would contribute to the product shape-selectivity in the MTO reaction.

The comprehensive analysis for diffusion of alkanes (methane, ethane and propane) within cavity-type molecular sieves demonstrated the strong correlation of inter-cavity diffusion and cavity structure, leading to the cognition of cavity-controlled diffusion. This indicates that the application of cavity-type and 8-MR molecular sieves would change the light olefins distribution by the cavity structure variation of the catalysts. This has been clearly presented in the previous work, in which the critical intermediates identification, predominant reaction route determination, olefin precursor formation and product distribution in this kind of SAPO or zeolite catalysts with varied cavity type has been studied in detail [9,10]. Cavity-controlled shape selectivity has been revealed in these works. Beside the reaction aspect, the present study reveals the substantial role of cavity structure in the molecular mass transport inside the confined environments of molecular sieves, in which the cavity would control the diffusion of the guest molecules, including reactant or product molecules in varied reaction systems, therefore mass transport is the other essential aspect that must be considered in shape selectivity of catalysis.

4. Conclusions

As one of the important aspect of shape selective catalysis, mass transport in cavity-type molecular sieves with very close eight-membered ring (8-MR) windows and varied cavity structure was

presented by means of pulsed-field gradient (PFG) NMR and molecular dynamics (MD) simulations. The diffusion performances of alkanes within cavity-type molecular sieves with the diffusion rate order of DNL-6 (RHO) > SAPO-34 (CHA) > SAPO-35 (LEV), are correlated to the cavity structure of the 8-MR SAPO molecular sieves. Diffusion feasibility is theoretically evaluated by tracing guest molecule along the diffusion path. Inter-cavity hopping process is visually displayed and is employed to describe the diffusion behavior of methane in the cavity-type molecular sieves. For the first time, the jump frequency (f) and jump length (L) are extracted successfully from diffusion trajectories of methane via the continuous-time random-walk (CTRW) coarse-graining method, through which both the feasibility and distance of hopping process are quantitatively disclosed to interpret the diffusion behavior in the cavity-type molecular sieves at the microscopic level. The quick diffusion of methane in RHO is synergistically attributed to the high jump frequency and long jump length, which is closely related to the less restriction or confinement from the large *lta* cavity environment with 8-MR windows as well as the long distance of each jump between adjacent sites. In case of LEV, its lowest diffusion coefficient with the feature of the low jump frequency and short jump length results from the strong confinement or restriction of the small cavity structure with 8-MR windows as well as the short distance of adjacent cavities. The substantial role of cavity structure in mass transport in 8-MR and cavity-type molecular sieves discloses the cavity-controlled diffusion in this kind of microporous materials. Cavity-controlled diffusion, together with the established cavity-controlled reaction will deepen and enrich the mechanism understanding of shape selective reaction and help to propose the optimized reaction strategy in the field of zeolite applications.

Acknowledgement

This paper is dedicated to the 70th anniversary of the Dalian Institute of Chemical Physics, Chinese Academy of Sciences. The authors thank the financial support from the National Natural Science Foundation of China (21473182, 91545104, 91745109, 21422606, 21522310, 91645112), the Youth Innovation Promotion Association of the Chinese Academy of Sciences (2014165), the Key Research Program of Frontier Sciences, Chinese Academy of Sciences (QYZDY-SSW-JSC024 and QYZDB-SSW-SLH026), International Partnership Program of Chinese Academy of Sciences (121421KYSB20180007), Strategic Priority Research Program of the Chinese Academy of Sciences (XDB10020202 and XDA21030200) and LiaoNing Revitalization Talents Program (XLYC1807227).

Declaration of Competing Interest

The authors declare no competing financial interest.

Appendix A. Supplementary material

Supplementary data to this article can be found online at <https://doi.org/10.1016/j.jcat.2019.07.010>.

References

- [1] M. Dusselier, M.E. Davis, *Chem. Rev.* 118 (2018) 5265–5329.
- [2] M. Moliner, C. Martínez, A. Corma, *Chem. Mater.* 26 (2014) 246–258.
- [3] U. Olsbye, S. Svelle, M. Børjgen, P. Beato, T.V.W. Janssens, F. Joensen, S. Bordiga, K.P. Lillerud, *Angew. Chem. Int. Ed.* 51 (2012) 5810–5831.
- [4] G. Sastre, A. Corma, *J. Mol. Catal. A: Chem.* 305 (2009) 3–7.
- [5] B. Smit, T.L.M. Maesen, *Chem. Rev.* 108 (2008) 4125–4184.
- [6] P. Tian, Y.X. Wei, M. Ye, Z.M. Liu, *ACS Catal.* 5 (2015) 1922–1938.
- [7] S.T. Xu, Y.C. Zhi, J.F. Han, W.N. Zhang, X.Q. Wu, T.T. Sun, Y.X. Wei, Z.M. Liu, *Adv. Catal.* 61 (2017) 37–122.
- [8] I. Yarulina, A.D. Chowdhury, F. Meirer, B.M. Weckhuysen, J. Gascon, *Nat. Catal.* 1 (2018) 398–411.
- [9] W.N. Zhang, J.R. Chen, S.T. Xu, Y.Y. Chu, Y.X. Wei, Y.C. Zhi, J.D. Huang, A.M. Zheng, X.Q. Wu, X.J. Meng, F.S. Xiao, F. Deng, Z.M. Liu, *ACS Catal.* 8 (2018) 10950–10963.
- [10] J.Z. Li, Y.X. Wei, J.R. Chen, S.T. Xu, P. Tian, X.F. Yang, B. Li, J.B. Wang, Z.M. Liu, *ACS Catal.* 5 (2015) 661–665.
- [11] I. Pinilla-Herrero, U. Olsbye, C. Marquez-Alvarez, E. Sastre, *J. Catal.* 352 (2017) 191–207.
- [12] Y. Bhowe, M. Moliner-Marin, J.D. Lunn, Y. Liu, A. Malek, M. Davis, *ACS Catal.* 2 (2012) 2490–2495.
- [13] J.R. Chen, J.Z. Li, Y.X. Wei, C.Y. Yuan, B. Li, S.T. Xu, Y. Zhou, J.B. Wang, M.Z. Zhang, Z.M. Liu, *Catal. Commun.* 46 (2014) 36–40.
- [14] J.Z. Li, Y.X. Wei, J. Chen, P. Tian, X. Su, S.T. Xu, Y. Qi, Q.Y. Wang, Y. Zhou, Y.L. He, Z.M. Liu, *J. Am. Chem. Soc.* 134 (2012) 836–839.
- [15] S.T. Xu, A.M. Zheng, Y.X. Wei, J.R. Chen, J.Z. Li, Y.Y. Chu, M.Z. Zhang, Q.Y. Wang, Y. Zhou, J.B. Wang, F. Deng, Z.M. Liu, *Angew. Chem. Int. Ed.* 52 (2013) 11564–11568.
- [16] I.M. Dahl, S. Kolboe, *J. Catal.* 149 (1994) 458–464.
- [17] W.G. Song, J.F. Haw, J.B. Nicholas, C.S. Heneghan, *J. Am. Chem. Soc.* 122 (2000) 10726–10727.
- [18] W. Song, H. Fu, J.F. Haw, *J. Am. Chem. Soc.* 123 (2001) 4749–4754.
- [19] T. Xu, J.L. White, U. S. Patent 6,743,747, 2004 (Priority Filing and PCT Published February 24, 2000).
- [20] T. Xu, J.L. White, U. S. Patent 6,734,330, 2004 (Priority Filing and PCT Published July 13, 2000).
- [21] J. Goetze, F. Meirer, I. Yarulina, J. Gascon, F. Kapteijn, J. Ruiz-Martínez, B.M. Weckhuysen, *ACS Catal.* 7 (2017) 4033–4046.
- [22] K.Y. Lee, H.-J. Chae, S.-Y. Jeong, G. Seo, *Appl. Catal. A: Gen.* 369 (2009) 60–66.
- [23] D. Chen, K. Moljord, A. Holmen, *Microporous Mesoporous Mater.* 164 (2012) 239–250.
- [24] Z.Q. Liu, Y.Y. Chu, X.M. Tang, L. Huang, G.C. Li, X.F. Yi, A.M. Zheng, *J. Phys. Chem. C* 121 (2017) 22872–22882.
- [25] B.P.C. Hereijgers, F. Bleken, M.H. Nilsen, S. Svelle, K.-P. Lillerud, M. Børjgen, B. M. Weckhuysen, U. Olsbye, *J. Catal.* 264 (2009) 77–87.
- [26] Y.F. Shen, T.T. Le, D.L. Fu, J.E. Schmidt, M. Filez, B.M. Weckhuysen, J.D. Rimer, *ACS Catal.* 8 (2018) 11042–11053.
- [27] A. Ghysels, S.L.C. Moors, K. Hemelsoet, K. De Wispelaere, M. Waroquier, G. Sastre, V. Van Speybroeck, *J. Phys. Chem. C* 119 (2015) 23721–23734.
- [28] M.K.F. Abouelnasr, B. Smit, *Phys. Chem. Chem. Phys.* 14 (2012) 11600–11609.
- [29] R. Krishna, J.M. van Baten, *Microporous Mesoporous Mater.* 137 (2011) 83–91.
- [30] G. Sastre, *Catal. Today* 226 (2014) 25–36.
- [31] N. Hedin, G.J. DeMartin, W.J. Roth, K.G. Strohmaier, S.C. Reyes, *Microporous Mesoporous Mater.* 109 (2008) 327–334.
- [32] J. Kärger, *ChemPhysChem* 16 (2015) 24–51.
- [33] D. Schneider, D. Mehlhorn, P. Zeigermann, J. Kärger, R. Valiullin, *Chem. Soc. Rev.* 45 (2016) 3439–3467.
- [34] R. Krishna, *Chem. Soc. Rev.* 41 (2012) 3099–3118.
- [35] P. Kortunov, S. Vasenkov, J. Kärger, R. Valiullin, P. Gottschalk, M. Fé Elia, M. Perez, M. Stöcker, B. Drescher, G. McElhiney, C. Berger, R. Gläser, J. Weitkamp, *J. Am. Chem. Soc.* 127 (2005) 13055–13059.
- [36] A.C. Forse, M.I. Gonzalez, R.L. Siegelman, V.J. Witherspoon, S. Jawahery, R. Mercado, P.J. Milner, J.D. Martell, B. Smit, B. Blümich, J.R. Long, J.A. Reimer, *J. Am. Chem. Soc.* 140 (2018) 1663–1673.
- [37] P. Bai, E. Haldoupis, P.J. Dauenhauer, M. Tsapatsis, J.I. Siepmann, *ACS Nano* 10 (2016) 7612–7618.
- [38] B. Li, P. Tian, J.Z. Li, J.R. Chen, Y.Y. Yuan, X. Su, D. Fan, Y.X. Wei, Y. Qi, Z.M. Liu, *Chin. J. Catal.* 34 (2013) 798–807.
- [39] A.M. Prakash, S. Unnikrishnan, *J. Chem. Soc., Faraday Trans.* 90 (1994) 2291–2296.
- [40] P.F. Wu, M. Yang, W.N. Zhang, S. Zeng, M.B. Gao, S.T. Xu, P. Tian, Z.M. Liu, *Chin. J. Catal.* 39 (2018) 1511–1519.
- [41] J.P. van den Berg, J.P. Wolthuisen, A.D.H. Clague, G.R. Hays, R. Huis, J.H.C. van Hooff, *J. Catal.* 80 (1983) 130–138.
- [42] A.G. Stepanov, M.V. Luzgin, V.N. Romannikov, V.N. Sidelnikov, E.A. Paukshtis, *J. Catal.* 178 (1998) 466–477.
- [43] R.M. Cotts, M.J.R. Hoch, T. Sun, J.T. Markert, *J. Magn. Reson.* (1969–1992) 83 (1989) 252–266.
- [44] B.-T.L. Bleken, K.P. Lillerud, T. Splith, A.-K. Pusch, F. Stallmach, *Microporous Mesoporous Mater.* 182 (2013) 25–31.
- [45] J. Kärger, D.M. Ruthven, D.N. Theodorou, *Diffusion in Nanoporous Materials*, Wiley-VCH, Weinheim, 2012.
- [46] C. Baerlocher, L.B. McCusker, *Database of Zeolite Structures*, 2016. <http://www.iza-structure.org/databases/>.
- [47] J.D. Gale, *J. Phys. Chem. B* 102 (1998) 5423–5431.
- [48] M.J. Sanders, M. Leslie, C.R.A. Catlow, *J. Chem. Soc., Chem. Commun.* (1984) 1271–1273.
- [49] S.E. Jee, D.S. Sholl, *J. Am. Chem. Soc.* 131 (2009) 7896–7904.
- [50] W. Smith, T.R. Forester, *J. Mol. Graphics* 14 (1996) 136–141.
- [51] D. Bermúdez, G. Sastre, *Theor. Chem. Acc.* 136 (2017) 116.
- [52] G. Sastre, A. Corma, *J. Phys. Chem. C* 113 (2009) 6398–6405.
- [53] D. Frenkel, B. Smit, *Understanding Molecular Simulations: From Algorithms to Applications*, Academic Press, San Diego, 2002.

- [54] G. Sastre, C.R.A. Catlow, A. Corma, *J. Phys. Chem. B* 103 (1999) 5187–5196.
- [55] D. Dubbeldam, S. Calero, D.E. Ellis, R.Q. Snurr, *Mol. Simulat.* 42 (2016) 81–101.
- [56] Q. Zhang, T.M. Wu, C. Chen, S. Mukamel, W. Zhuang, *Proc. Natl. Acad. Sci. U.S.A.* 114 (2017) 10023–10028.
- [57] J. Kärger, H. Pfeifer, *Zeolites* 7 (1987) 90–107.
- [58] E. Beerdsen, D. Dubbeldam, B. Smit, *J. Phys. Chem. B* 110 (2006) 22754–22772.
- [59] R. Krishna, J.M. van Baten, *Chem. Eng. Technol.* 30 (2007) 1235–1241.
- [60] J. Caro, M. Bulow, W. Schirmer, J. Karger, W. Heink, H. Pfeifer, S.P. Zdanov, *J. Chem. Soc. Faraday Trans. I* (81) (1985) 2541–2550.
- [61] J. Kärger, H. Pfeifer, F. Stallmach, N.N. Feoktistova, S.P. Zhdanov, *Zeolites* 13 (1993) 50–55.
- [62] Y.G. Chung, P. Bai, M. Haranczyk, K.T. Leperi, P. Li, H.D. Zhang, T.C. Wang, T. Duerinck, F.Q. You, J.T. Hupp, O.K. Farha, J.I. Siepmann, R.Q. Snurr, *Chem. Mater.* 29 (2017) 6315–6328.
- [63] C.B. Fan, Z.Q. Liu, L.L. Gong, A.M. Zheng, L. Zhang, C.S. Yan, H.Q. Wu, X.F. Feng, F. Luo, *Chem. Commun.* 53 (2017) 763–766.
- [64] P. Bharathi, R.C. DeKa, S. Sivasanker, R. Vetrivel, *Catal. Lett.* 55 (1998) 105–112.
- [65] R.Ch. DeKa, R. Vetrivel, *J. Catal.* 174 (1998) 88–97.
- [66] L.T. Bu, M.R. Nimlos, D.J. Robichaud, S. Kim, *J. Phys. Chem. C* 121 (2017) 500–510.
- [67] J. Qvist, H. Schober, B. Halle, *J. Chem. Phys.* 134 (2011).
- [68] W.L. Dai, M. Scheibe, L.D. Li, N.J. Guan, M. Hunger, *J. Phys. Chem. C* 116 (2012) 2469–2476.